Frequency and Power Measurements on the Harmonic Recirculating Planar Magnetron

Drew A. Packard, *Student Member, IEEE*, Steven C. Exelby, *Student Member, IEEE*, Nicholas M. Jordan, *Senior Member, IEEE*, Christopher J. Swenson, *Student Member, IEEE*, Brad W. Hoff, *Senior Member, IEEE*, Y. Y. Lau, *Fellow, IEEE*, and Ronald M. Gilgenbach, *Life Fellow, IEEE*

***Abstract*— The harmonic recirculating planar magnetron (HRPM) is a frequency-agile, multispectral HPM source. The HRPM implements an *L*-band oscillator (LBO) and an *S*-band oscillator (SBO) near 1 and 2 GHz, respectively. The novel coaxial-all-cavity-extraction (CACE) method was implemented to extract power from the SBO. The two oscillators demonstrated harmonic frequency locking, where the SBO frequency locked to the LBO second harmonic frequency. The two oscillators are concluded to operate as a damped, driven, harmonic oscillator system. In the locked state, the LBO acts as the driving oscillator, the SBO acts as the driven oscillator, and the coupling mechanism between the two oscillators is the harmonic content in the electron spokes as they propagate directly from the LBO to the adjacent SBO. The two primary variables studied in this system are the LBO harmonic frequency and the SBO quality factor, Q. In isolated SBO experiments, the dominant operating state of the magnetron was the $5\pi/6$ mode. However, when operated in tandem with the LBO, the SBO was forced to operate in the π-mode. Output powers in HRPM experiments generated SBO powers of 9.5 ± 1.4 MW at high Q, 19 ± 6 MW at moderate Q, and 28 ± 9 MW at low Q. Output powers in the isolated SBO configuration were not significantly different from the HRPM. By experimentally manipulating the hub drift direction and altering the evolution of harmonic content received by the SBO, the locked state was significantly diminished, suggesting that the beam spokes play a crucial role.**

***Index Terms*— Frequency harmonics, frequency locking, high-power microwaves (HPM), radio frequency extraction, relativistic magnetron.**

I. Introduction and Motivation

MAGNETRONS are microwave oscillators used in a range of applications, spanning from fundamental science to defense and medical technologies. For defense applications, relativistic magnetrons are of particular interest as sources of high-power microwaves (HPMs) [1]–[4]. Tens of millions of magnetrons are manufactured annually for use in systems ranging from microwave ovens to radar because they are uniquely compact, energy dense, and highly efficient [5]. The relativistic magnetron [6], [7] satisfies the specific need for very high RF power generation, reaching as high as Gigawatt level output powers. A limitation of the magnetron is that it is narrowband, often designed to generate a single frequency. This is undesirable in systems designed to deliver energy to a target that may couple more strongly to electromagnetic radiation in one frequency band than another. To expand the frequency range of a conventional magnetron, one solution is operation in different modes on the anode slow-wave structure (SWS) [8]. This can be achieved by altering the operating voltage or applied magnetic field, but in practice, these are often held constant.

Magnetrons are commonly made frequency agile by introducing tuning methods to mechanically change the electromagnetic boundary conditions, and, thus, the resonant frequency, of the anode SWS. Tuning ranges up to 33% have been demonstrated [9]. However, this mechanical change still limits the magnetron to operate at a single frequency on the microsecond scale. To produce multiple frequencies simultaneously with a single source, one viable solution is to use multiple SWSs. This approach has been applied to magnetically insulated line oscillators, traveling wave tubes, and backward wave oscillators [10]–[12].

Contrary to the conventional magnetron, often marked by a central cylindrical cathode and surrounding cylindrical anode with an azimuthally symmetric SWS, University of Michigan (UM) investigators invented the recirculating planar magnetron (RPM) [13]–[15]. The RPM geometry recirculates the Brillouin hub using two cylindrical bends that connect planar regions on opposite sides of a planar cathode. This approach elongates the cathode-emitting surface, enabling it to emit larger currents in the space-charge-limited regime where HPM sources are often operated. Furthermore, the opposing planar regions on the anode allow for the implementation of two different SWSs synchronized to the same beam velocity. This enabled the multifrequency RPM (MFRPM) [16], [17] to become the first magnetron to simultaneously produce multiple frequencies. The MFRPM implements an *L*-band oscillator (LBO) and an *S*-band oscillator (SBO), specifically designed for operation near 1 and 2 GHz, respectively. The MFRPM is also the first such magnetron to demonstrate

Manuscript received November 15, 2019; revised April 21, 2020; accepted April 27, 2020. This work was supported in part by the U.S. Office of Naval Research under Grant N000014-16-1-2353. The review of this article was arranged by Senior Editor D. A. Shiffler. *(Corresponding author: Drew A. Packard.)*

Drew A. Packard, Nicholas M. Jordan, Christopher J. Swenson, Y. Y. Lau, and Ronald M. Gilgenbach are with the Department of Nuclear Engineering and Radiological Sciences, University of Michigan, Ann Arbor, MI 48109 USA (e-mail: drupac@umich.edu).

Steven C. Exelby and Brad W. Hoff are with the Air Force Research Laboratory, Kirtland Air Force Base, Albuquerque, NM 87123 USA.

Color versions of one or more of the figures in this article are available online at http://ieeexplore.ieee.org.

Digital Object Identifier 10.1109/TPS.2020.2991656

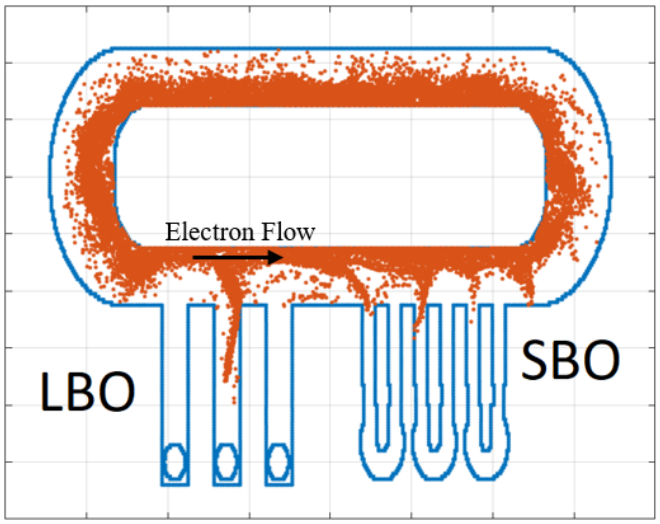

Fig. 1. Particle-in-cell simulation of the HRPM in ICEPIC, showing spoke generation in the LBO and SBO regions. The spokes and their harmonic content are much better preserved in the planar drift region between the two oscillators, whereas they are significantly dispersed after traveling around the recirculating bend following the SBO.

harmonic frequency locking [18], a phenomenon where the SBO resonant frequency locked to the second harmonic of the LBO operating frequency. When this locked state was discovered, it was theorized that the locking mechanism between the two oscillators was harmonic content in the beam spokes passed from the LBO to the SBO via the recirculating bend. However, this device was not frequency tunable; without varying the magnetic field, the LBO and SBO were each capable of operating at a single frequency. Additionally, the MFRPM did not demonstrate the efficacy of a magnetron that could generate more than two frequencies. This is because the LBO and SBO were placed on opposite sides of the planar cathode; it did not conclusively demonstrate whether two planar oscillators at different frequency bands could reliably operate adjacent to each other with only a planar drift region between them.

The harmonic RPM (HRPM) was developed at UM to demonstrate the possibility of an even more robust multispectral magnetron. The two oscillators of the HRPM are placed adjacent to each other, on the same side of the cathode, with the opposing side of the anode left as a smooth-bore drift region. In a more advanced prototype, this drift region could be replaced with another set of oscillators scaled to operate at different frequencies from the opposing pair. Specifically designed to study and take advantage of harmonic frequency locking, the HRPM implements its own frequency-agile LBO and SBO. Its applied magnetic field is oriented such that the $\vec{E_{DC}} x \vec{B}$ drift velocity forces the electron hub and its harmonic content to travel directly from the LBO to the adjacent SBO, locking the SBO operating frequency to the tunable LBO. The shorter, planar drift region better preserves the spokes' harmonic content than the cylindrical recirculating bends through which the spokes in the MFRPM needed to traverse. The recirculating bends disperse and demodulate the spokes, reducing the harmonic content; this effect is evident in Fig. 1, as there are no spokes preserved in the planar drift region opposite to the cathode of the two oscillators. Furthermore, an additional oscillator tuned to the fourth harmonic of the LBO could theoretically be placed downstream and locked to the SBO. The HRPM serves as a prototype for a frequency-agile magnetron capable of producing four or more frequencies simultaneously at MW power levels.

II. Design and Cold Test

The concept of harmonic frequency locking is important because it strongly influences the design decisions made for the HRPM. Based on evidence from experiments on the MFRPM, it is hypothesized that the LBO and SBO of the HRPM will behave as a damped, driven, harmonic oscillator system. The driving oscillator is the LBO, and the driven oscillator is the SBO. The coupling mechanism between the two is thought to be the harmonic content in the beam spokes as they propagate from the LBO to SBO. Fig. 1 shows an Improved Concurrent Electromagnetic Particle in Cell Code (ICEPIC) [19], [20] simulation of the modulated beam drifting from the LBO to SBO.

The driving oscillator (LBO) delivers an excitation or driving frequency to the driven oscillator (SBO); in the HRPM, the driving frequency is the LBO's second harmonic. The driven oscillator will, when operating independently, oscillate at a particular mode-dependent, free-running frequency. When the SBO is driven exactly at its π-mode free-running frequency, it is expected to generate maximum power output. However, when there is some difference between the driving frequency and the driven oscillator's free-running frequency, the driven oscillator is expected to oscillate at the excitation frequency and simply generate less output power. The frequency range wherein the oscillators lock is determined by the quality factor (Q) of the mode being excited.

Ultimately, to test the driven oscillator hypothesis and gain more insight into harmonic frequency locking, the HRPM was designed with two specific, controlled variables in mind: driving frequency and total quality factor.

The driving frequency is varied to determine the locked bandwidth between the LBO and SBO. Thus, the LBO was designed with frequency agility in mind. Fig. 2(b) depicts the anode from the point of view of the cathode and demonstrates how frequency agility is achieved using cylindrical tuners. They are located in the back of the LBO cavities and designed to plunge downward from the top of the anode, with the depth of their penetration denoted by the variable L. With this tuner, the LBO frequency can be adjusted on a shot-by-shot basis.

The other variable of interest is the total quality factor, Q_t, of the mode targeted for locking on the SBO. By decreasing Q_t, the bandwidth of the mode increases; in doing this, the harmonic locked bandwidth is predicted to increase as well. The Q_t can be decreased by increasing the coupling between the extractor and the SBO. In the HRPM, this is controlled by the length, h, of the coupling aperture, shown in Fig. 2(b), connecting the SBO cavities to its extractor. Three different versions of the SBO were fabricated and tested, all with different values of h, with the intent of performing experiments at high Q_t, moderate Q_t, and low Q_t.

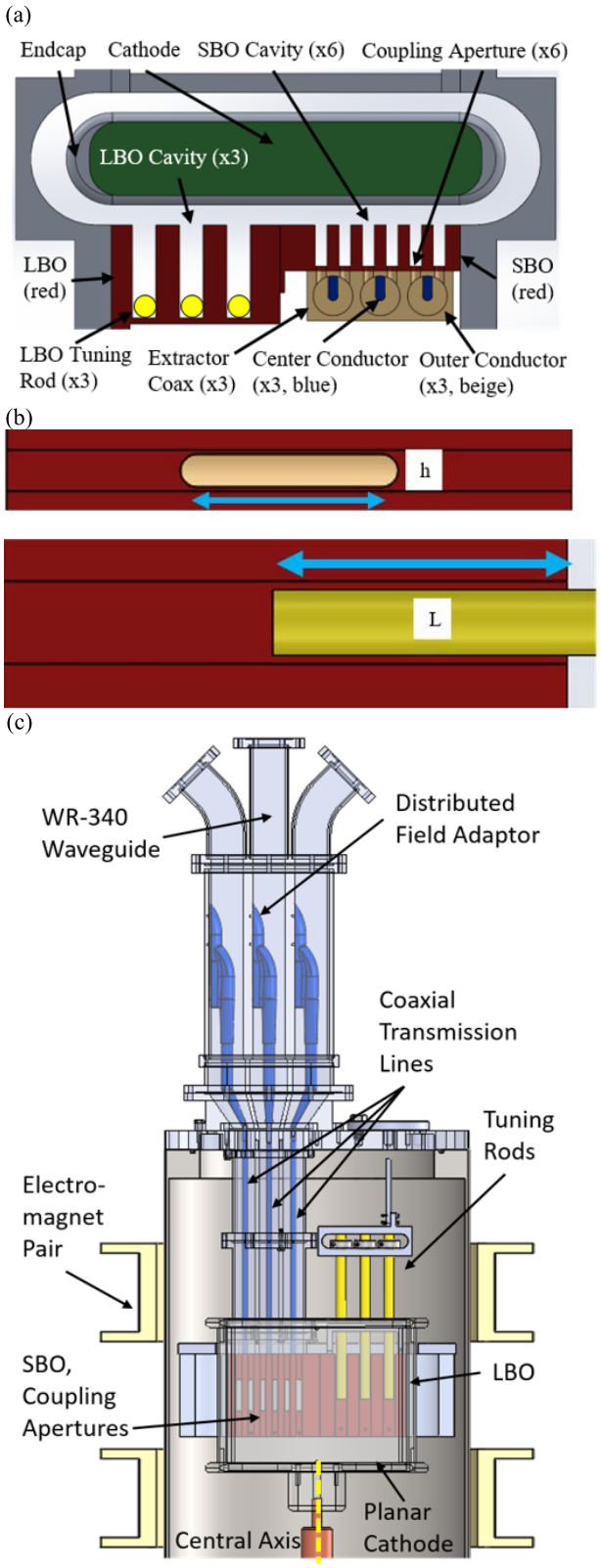

Fig. 2. (a) Top-down cross section of the HRPM. (b) Unit cells of the SBO (top) and LBO (bottom) cavities, pictured from the view of the cathode. The two independent variables are illustrated: the aperture length h and tuning rod depth L. (c) Cross section of the entire experimental assembly with several components transparent. The tuning stubs plunge downward into the cavities, translating along the central axis.

Due to physical limitations introduced by the inner radius of the electromagnets and vacuum chamber, some design concessions were made. There was not ample physical space to extract microwave power from both planar oscillators and maintain frequency agility on the LBO. In the interest of investigating harmonic frequency locking, it was decided that extraction of microwave power from the SBO was more pertinent than extraction from the LBO.

Thus, coaxial-all-cavity-extraction (CACE) was implemented on the SBO [21]. The extractor is designed for operation in the π-mode, where the electric field tangent to the flow of electrons advances 180° per cavity. Such a field pattern can excite a transverse electromagnetic (TEM) wave in all three coaxial transmission lines (CTLs) simultaneously, each coupled to the SWS cavities through slots of length h. Other modes that may dominate and interact with the space charge will have one or more null cavities whose phase does not advance. One example is the $5\pi/6$ mode, whose field pattern does not advance in one of the two central cavities, resulting in weak excitation of a TEM wave in the central CTL. This may cause an uneven distribution of power in the CTLs, where the two outer lines propagate greater fractions of the power when compared with the π-mode. This could result in breakdown of one of the CTLs and significant physical damage to the extractor. The π-mode is best equipped to evenly distribute the power across all three lines, enabling safer operation near the Kilpatrick limit [22].

As the electromagnetic waves propagate down the transmission line, the smaller diameter coax is adapted to the larger diameter coax outside of the test chamber with a flared and tapered adaptor. The larger diameter portion of coax is then adapted to waveguide with a distributed field adaptor (DFA), originally designed for use in RPM-CACE [21]. The DFA has a passband in the range of 1.85–2.2 GHz. Finally, the extracted microwave energy is measured with a directional coupler, and each waveguide is terminated with a microwave load.

The spacing between adjacent cavities, or circuit pitch, of both oscillators was largely determined by the DFA passband and inner diameter of the test chamber. The magnetic field necessary for interaction between the SWSs and the space charge hub is determined by the Buneman–Hartree condition [23] stated in (1). The relevant parameters are the gap voltage, V_{BH}, magnetic field, B, electron mass, m, speed of light, c, elementary charge, e, AK-gap distance, D, and normalized SWS phase velocity, $v_{\mathrm{ph}}/c \equiv \beta$

$$V_{\mathrm{BH}} = \beta B D c - \frac{mc^2}{e}\left(1 - \sqrt{1-\beta^2}\right). \tag{1}$$

In this application, it is desirable to minimize the required magnetic field to ensure the electromagnets can provide the necessary field strength. While maintaining synchronism between the SWS and space charge hub, the lowest magnetic field possible corresponds to the fastest SWS phase velocity allowed by the application. The phase velocity, v_{ph}, is determined by the mode of operation, oscillation frequency, and circuit pitch, according to the following equation:

$$v_{\mathrm{ph}} = \omega/\beta = \frac{2\pi f}{(\varphi/P)}. \tag{2}$$

The relevant variables are the circuit pitch, P, frequency, f, angular frequency, ω, wavenumber, β, and advancement of the phase in the tangential electric field per unit cell, φ.

The most desirable mode is the π-mode, so the phase velocity can only be increased by raising the frequency or circuit pitch. The maximum allowed frequency is determined by the upper frequency limit of the DFA, and the maximum possible circuit pitch is determined by the diameter of the vacuum chamber and electromagnets. Thus, for the SBO, the largest circuit pitch considered possible with a 6-cavity array was determined to be 1.6 cm. The electromagnetic solver high-frequency structure simulator (HFSS) was used to determine the cavity length necessary (2.8 cm) to set the π-mode frequency near 2.2 GHz, which is the upper edge of the DFA passband.

The LBO was designed knowing the phase velocity, frequency, and circuit pitch of the SBO. To synchronize with the same electron beam as the SBO, the LBO must have the same phase velocity. To test the driven oscillator hypothesis, its oscillation frequency, when tuned correctly, must be half of that of the SBO. This ultimately means its circuit pitch must double that of the SBO. The LBO cavity length and tuner parameters were determined in HFSS to provide a large range of available frequencies to excite the SBO. The number of LBO cavities was set to three upon consideration of the results obtained from particle-in-cell solvers CST-Particle Studio [24] and ICEPIC, although it may have been possible to reduce the number of cavities to two. Four or more cavities were avoided due to the size constraints previously outlined and to reduce the possibility of mode competition with the desired π-mode.

It is expected that the quality factor will behave in accordance with the following equation, where Q_t is the total quality factor, Q_u is the unloaded quality factor, and Q_{ext} is the external quality factor [25]:

$$\frac{1}{Q_t} = \frac{1}{Q_u} + \frac{1}{Q_{\text{ext}}}. \tag{3}$$

The unloaded quality factor arises from ohmic losses due to the finite conductivity of the SWS and radiative losses. During the experiment, the HRPM rests in an electrically large test chamber that may allow some portion of the electromagnetic energy generated in the cavities to radiate out. However, Q_u is not expected to change when h is varied. When h is increased, the quality factor presented by the extractor Q_{ext} is expected to decrease, thus resulting in decreased Q_t and increased output power.

Cold tests were performed on the HRPM with an HP 8722D vector network analyzer to assess the frequency and quality factor of relevant resonant modes. The two outer SBO waveguides were excited and S_{21} was measured. Resonant modes result in peaks on each S_{21} measurement; the labeled local maxima in Fig. 3(a) are modes on the SWS identified using HFSS. A similar method was performed with the LBO by exciting recessed microwave B-dot loops in the two outer cavities and measuring S_{21} to find the resonant π-mode peak. Fig. 3(b) plots the LBO cold test harmonic frequency and overlays the SBO π-mode cold test frequency for each quality factor tested. The LBO frequency is linear in the region where

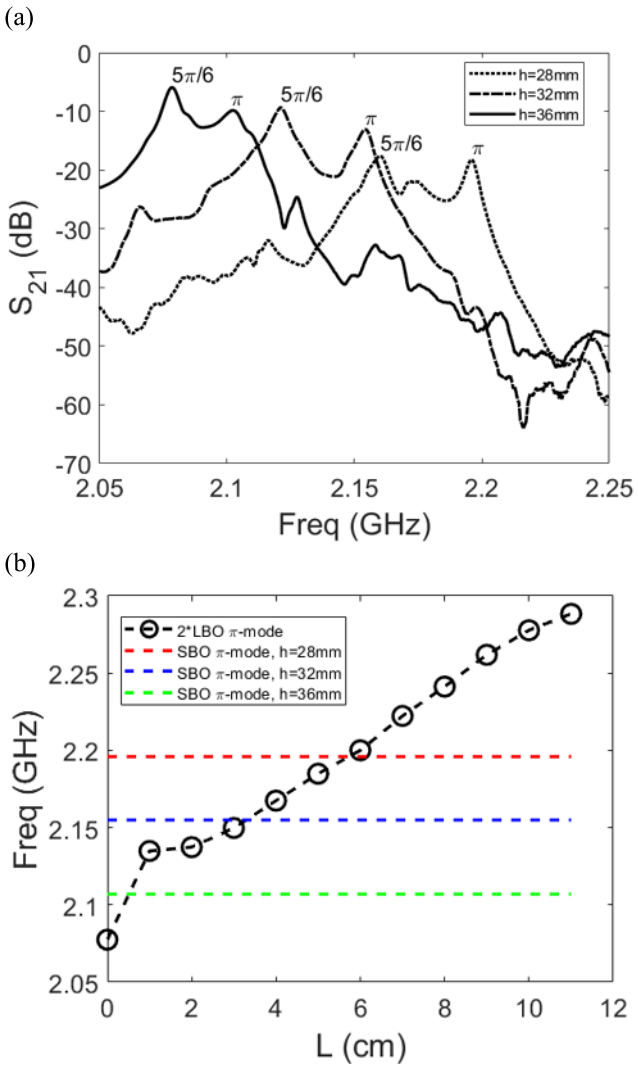

Fig. 3. (a) For each value of h, S_{21} is measured by exciting the two outer waveguides of the SBO extractor. Prominent peaks are observed for the π-mode and $5\pi/6$ mode. (b) LBO cold test harmonic frequencies as a function of tuner position (circles) with SBO π-mode frequency plotted for each value of Q_t (dashed lines). With beam loading, it is expected that the targeted SBO modes will fall in the preferred, linear LBO tuning range of 2–11 cm.

L ranges from 2 to 11 cm, and it is, therefore, preferred to operate in this range. Due to beam loading, the LBO hot test harmonic frequency is expected to decrease more than the SBO frequency, pushing the targeted modes further into the preferred tuning range.

The total quality factor and cold test frequency of the relevant resonant modes on the SBO were determined with the 3-dB method [26] as h was varied from the data given in Fig. 3(a) and are shown in Table I. Significantly, the π-mode quality factor monotonically decreases as expected, while the $5\pi/6$-mode quality factor is relatively unaffected. The resonant frequency of both modes decreases in each case, as they are further loaded by the extractor.

III. HRPM Experiments

HRPM hot test experiments were driven by the Michigan Electron Long Beam Accelerator-Ceramic Insulator (MELBA-C) at −300 kV, drawing roughly 1 kA at generation

TABLE I

COLD TEST QUALITY FACTOR AND FREQUENCY OF THE RELEVANT MODES MEASURED IN HOT TEST, LISTED AS A FUNCTION OF THE SLOT LENGTH h. THE π-MODE QUALITY FACTOR MONOTONICALLY DECREASES WITH h, WHILE THE $5\pi/6$ QUALITY FACTOR IS RELATIVELY UNAFFECTED

h_n (mm)	5π/6-mode		π-mode	
	f (GHz)	Q_t	f (GHz)	Q_t
$h_1 = 28$	2.158	270	2.196	440
$h_2 = 32$	2.121	260	2.155	240
$h_3 = 36$	2.084	290	2.107	140

of peak microwave power. Voltage is applied for pulse lengths of 300–500 ns. This configuration is expected to give more insight on the driven oscillator hypothesis with respect to harmonic frequency locking. Experiments with the aperture length set to h_1 (high Q_t), h_2 (moderate Q_t), and h_3 (low Q_t) were performed at a single magnetic field of 0.308, 0.284, and 0.283 T, respectively. The LBO frequency, SBO frequency, and output power were determined using the following processes.

To determine SBO output power and frequency, each of the three output waveguides feed their own directional coupler whose output signal is then split into two different components. One signal is passed through a calibrated HP 8472B Low-Barrier Schottkey Diode (0.3-dB precision) into an oscilloscope for measuring power; the other raw signal is measured directly by a 6-GHz, 20-GSa/s Agilent 58455A oscilloscope. Directly sampled signals undergo Fourier analysis to determine a dominant frequency for each SBO waveguide output. For each shot, a single composite SBO frequency is determined as the arithmetic mean of the dominant frequency from each of the three sampled signals, that is, $f_{comp} = (f_1 + f_2 + f_3)/3$. Sample signals for both the SBO and LBO and their Fourier transform data are given in Fig. 4.

The LBO frequency is sampled using the same microwave B-dot loops used in cold test. The output signals are directly sampled at 20 GSa/s. The dominant frequency of all LBO B-dot outputs is determined with Fourier analysis. A single, composite LBO frequency is determined for every shot as the arithmetic mean of the dominant frequency from all available B-dot signals. This distinction is made because different numbers of B-dot probes were available for the high, moderate, and low Q experiments. The high Q experiment only sampled the middle LBO cavity. Probes were placed in all three LBO cavities for the moderate Q experiment, but the cables used to sample the B-dots in the two outer cavities were destroyed at different points in the experiment by axial endloss from the cathode. Finally, in the low Q experiment, after garnering some experience from the two previous experiments, all three B-dots were sampled for every shot by adequately shielding their cables from endloss currents. Thus, in the low Q experiment, a single composite LBO frequency is determined for every shot as the arithmetic mean of the dominant frequency from each of the three sampled signals; in the same manner as the SBO, $f_{\text{comp}} = (f_1 + f_2 + f_3)/3$. However, in the two other experiments, each composite frequency was determined by the arithmetic mean of one, two, or three signals, depending on how many probes were available for that specific shot.

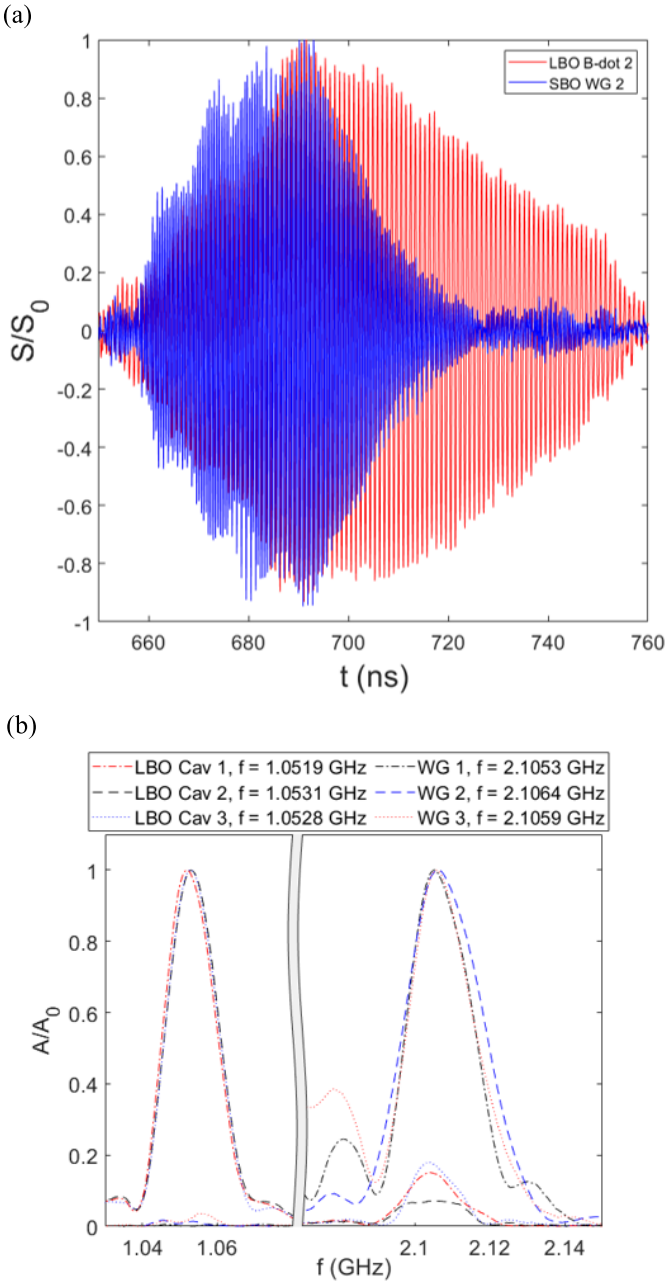

Fig. 4. Waveforms and Fourier transforms from MELBA shot 17 755, with $L = 4.5$ cm and $h = h_3$. (a) Normalized B-dot signal of the center LBO cavity is overlaid with the normalized waveguide signal from the center SBO output. The signals from the other two B-dots and waveguides are not shown. (b) Fourier transforms for the three LBO and SBO signals. The dominant peaks of all three LBO signals cluster near 1.053 GHz, while the SBO signals lock to the harmonic frequency near 2.105 GHz. Notice the smaller harmonic peaks from the LBO also located near 2.105 GHz. For both the LBO and SBO, the composite frequency is the arithmetic mean of all signals that were measured. In this shot, the LBO composite frequency is 1.0526 GHz, its composite harmonic frequency is 2.1052 GHz, and the SBO composite frequency is 2.1059 GHz.

The output frequency results for the HRPM are shown in Fig. 5. At each tuner position L, multiple shots were taken. Each data point for the LBO harmonic frequency trend and SBO frequency trend represents the arithmetic mean of

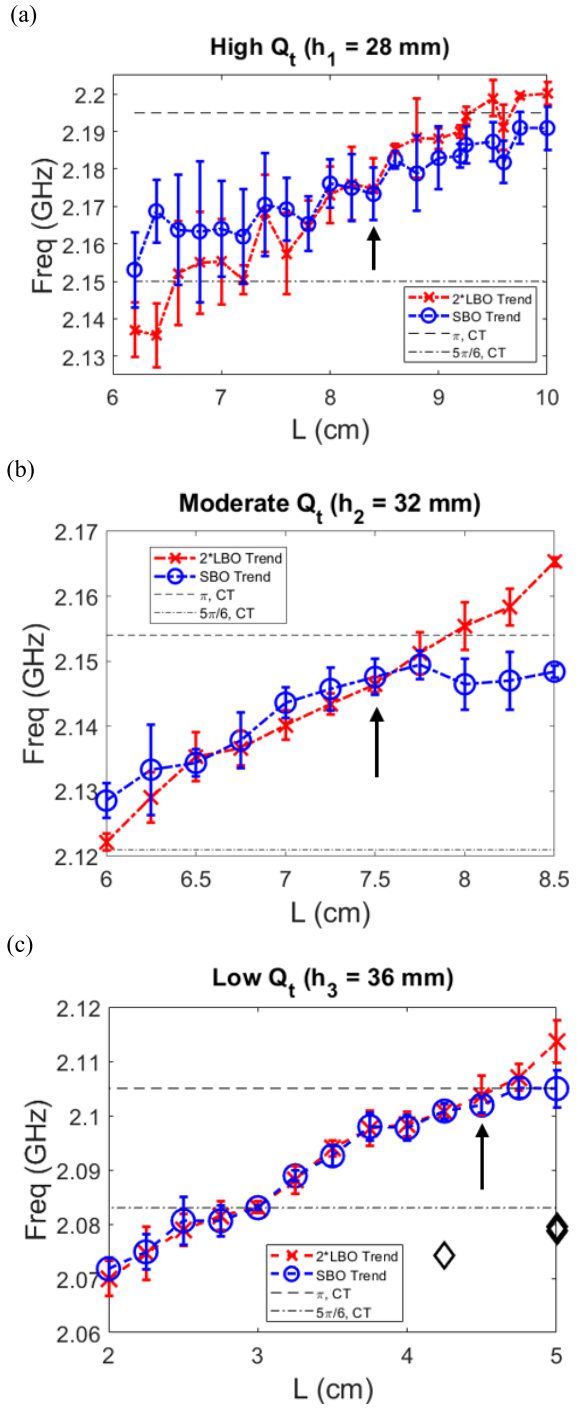

Fig. 5. LBO harmonic frequency and SBO frequency trends as a function of tuner length (L) for (a) high Q_t, (b) moderate Q_t, and (c) low Q_t. For each value of L, multiple shots were taken. The arithmetic mean of the set of composite frequencies at each value of L determines the plotted trends. Error bars extend one standard deviation from each data point. (c) Diamonds represent shots where the SBO exhibited drastically different operating frequencies in one of the outputs when compared with the other two. Operation in the π-mode is observed when the LBO is tuned to the appropriate value of L, and the arrows indicate the tuner position where maximum SBO output power was observed. In each case, maximum power was observed within 10 MHz of the free-running SBO π-mode frequency predicted by PIC simulations in CST-PS. The SBO frequency locks more consistently to the LBO harmonic frequency and over a wider range as the π-mode quality factor is decreased.

all composite frequencies taken at that specific value of L. That is, for the SBO, every data point is determined as $f_{\text{avg}} = (f_{\text{comp,1}} + f_{\text{comp,2}} + \ldots + f_{\text{comp,n}})/n$, where n is the number of shots taken at that value of L. For the LBO, the average dominant frequency for each value of L is determined with the same process. The plotted trend is the collection of the average frequencies, multiplied by two to get the average harmonic frequency. At each value of L, the standard deviation is calculated from the associated set of composite frequencies; the vertical error bars extend one standard deviation in each direction from the data point. All of this information is overlaid with the SBO $5\pi/6$- and π-mode cold test frequencies. The LBO is tuned across a range suitable for excitation of both the $5\pi/6$- and π-modes on the SBO. A total of 131, 88, and 93 shots were taken at high Q_t, moderate Q_t, and low Q_t, respectively. At low Q_t, a total of seven shots demonstrated significant mode competition between the π and $4\pi/6$ modes to the point where each was dominant in one or two waveguides but not all three. For reference, three of these shots are displayed separately in Fig. 5(c) in diamonds. The others are removed for plotting purposes.

As the tuner depth is increased, the LBO harmonic frequency increases as expected from the cold test results of Fig. 3(b). For each quality factor tested, the SBO demonstrates harmonic frequency locking with the LBO harmonic frequency across a certain range of L. Furthermore, the SBO frequency can be controlled across a wider range as the quality factor decreases, which is consistent with the driven oscillator hypothesis.

This is an important result; by correctly adjusting its quality factor, the SBO is made frequency agile due to the presence of the LBO. Judging from Fig. 5, the locked ranges are 2.165–2.182 GHz at high Q_t, 2.134–2.149 GHz at moderate Q_t, and 2.072–2.105 GHz at low Q_t. Additionally, as the total quality factor is decreased across the three experiments, both the SBO and LBO frequencies track in a more consistent and linear fashion with the tuner length. The error bars significantly decrease across the tested range of L as the quality factor is decreased, demonstrating increased shot-to-shot consistency due to harmonic frequency locking.

Significantly, the SBO was observed to operate in π-mode in the HRPM geometry, whereas π-mode was not observed as a dominant mode in the isolated SBO experiment (to be presented later). This is demonstrated in Fig. 5, where at certain tuner positions, the SBO output frequency can be tuned to agree more with the π-mode than $5\pi/6$-mode cold test frequencies. This is another important result, as it shows the introduction of an upstream LBO can be used as a form of mode control on the SBO.

The SBO demonstrated some interesting behavior in unlocked portions of the tuning range as well. First, consider Fig. 5(a) where L ranges from 6.2 to 7.6 cm. The SBO average frequency does not agree with any mode observed in cold test. This is again because the output frequencies in each waveguide were significantly different from each other. In this range, for a given shot, the waveguide outputs corresponding to the center or right-most pair of cavities [referencing Fig. 2(a)] may demonstrate π- or $5\pi/6$-mode dominance. Meanwhile, the waveguide output corresponding to the pair of cavities

nearest to the LBO may demonstrate harmonic frequency locking. This results in a composite frequency that is neither harmonically locked nor consistent with any specific mode found in cold test. Because this behavior is inconsistent, large error bars are observed in this portion of the tuning range.

Additionally, consider Fig. 5(b), where π-mode operation is consistently demonstrated with L ranging from 8.0 to 8.5 cm in an *unlocked* state. In this range, the SBO hot test frequency of 2.147 GHz agrees well with the π-mode cold test frequency of 2.154 GHz, even as the LBO harmonic frequency continues to increase; the frequency difference is very likely due to beam loading. This region of unlocked operation shows that, even in the absence of harmonic frequency locking, the LBO strongly influences the operating mode of the SBO.

Finally, SBO output power is plotted in Fig. 6 as a function of the tuner position and total quality factor. The total microwave power is defined as the sum of the three output waveguides, and the peak power is the maximum of this total power pulse. The red Xs indicate individual shots, whereas the black circles and error bars represent the arithmetic mean and standard deviation of the peak power for all shots taken at that tuner position, respectively. First, note that the extracted power increases as the π-mode Q_t decreases, which is expected. Maximum power output of the SBO is observed with L set to 8.4, 7.5, and 4.5 cm at high Q_t, moderate Q_t, and low Q_t, respectively. At these optimal operating points, the SBO mean composite frequency was 2.173 GHz $\pm$ 7.1 MHz, 2.148 GHz $\pm$ 2.8 MHz, and 2.102 GHz $\pm$ 1.5 MHz. These points are marked in Fig. 5 with black arrows, each demonstrating optimal operation when the SBO is excited slightly below the π-mode cold test frequency. This is also consistent with the driven oscillator hypothesis: when π-mode is excited on resonance, maximum power output is observed. The π-mode free-running frequency, obtained from PIC simulations in CST-Particle Studio, was predicted to be 2.1775 GHz at high Q_t, 2.14 GHz at moderate Q_t, and 2.092 GHz at low Q_t. All these agree within 10 MHz to the mean composite frequency of the SBO where maximum power was observed, further suggesting that it was indeed being driven on resonance.

The output power is compared with isolated SBO in Table II; at high Q_t and moderate Q_t, the output power is not changed from isolated SBO to HRPM operation, whereas at low Q_t, the HRPM output power is approximately 25% lower than the isolated SBO experiment.

IV. Isolated SBO Experiments

Additional experiments were completed with a smooth-bore drift region in place of the LBO. In these isolated SBO experiments, the magnetic field was swept for each aperture length to determine its effect on the SBO operating mode and output power.

Fig. 7(a) depicts the frequency information from the isolated SBO hot test. The $4\pi/6$ and $5\pi/6$ modes were dominant in the isolated SBO experiment; significantly, the π-mode was not observed as a dominant mode. Thus, for each value of h that was tested, it was either the $4\pi/6$ or $5\pi/6$ mode that resonated

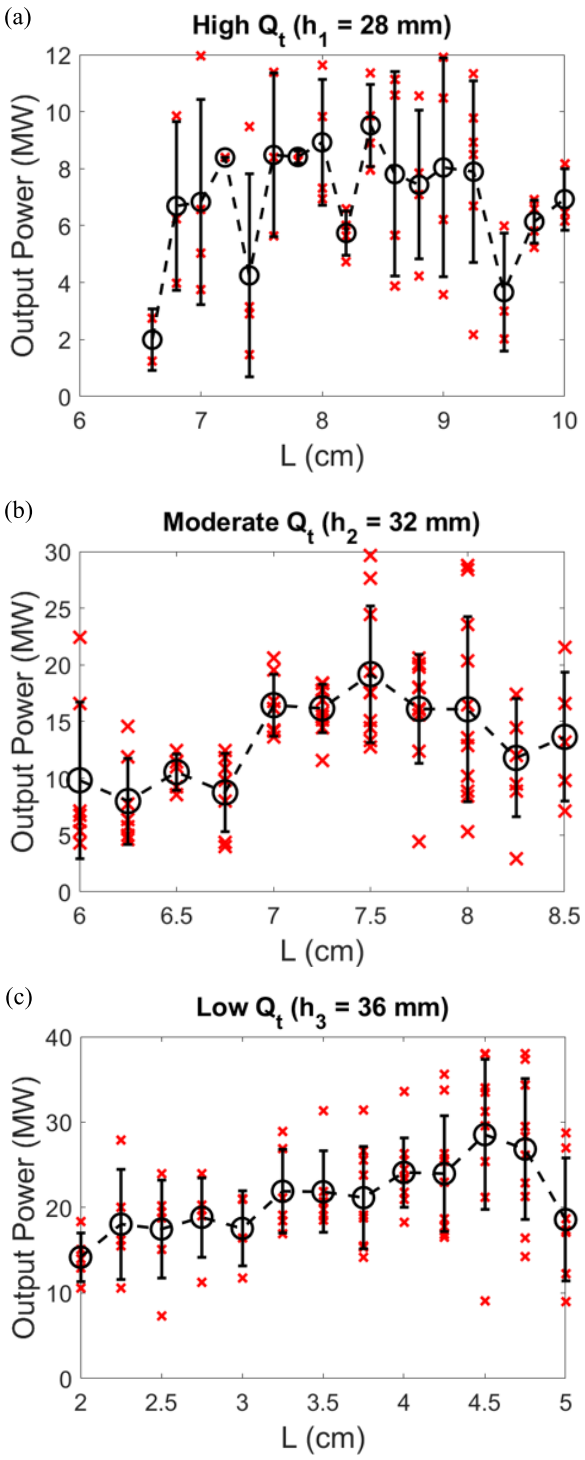

Fig. 6. SBO peak output power as a function of L for (a) high Q_t (h_1), (b) moderate Q_t (h_2), and (c) low Q_t (h_3). Red crosses indicate individual shots, and black circles indicate the arithmetic mean of all peak powers recorded for an individual value of L. The standard deviation was also calculated for each collection of shots at a given L. The spread is represented in the error bars, which extend one standard deviation in each direction. In each case, maximum power generation is observed when the SBO π-mode is excited 5–20 MHz beneath its cold test frequency, as indicated by the black arrows in Fig. 5. It is plausible that the π-mode free-running frequency would fall in such a range due to beam loading. Note that the vertical axes in each of these plots are different. This is because it is important to clearly demonstrate where maximum power is generated in each experiment. As h is increased and, thus, the π-mode Q_t is decreased (shown in Table I), the expected result of increased output power is observed.

TABLE II

COMPARISON OF OPERATION BETWEEN THE ISOLATED SBO EXPERIMENTS AND HRPM EXPERIMENTS. HRPM EXPERIMENTS DEMONSTRATED π-MODE DOMINANCE AT POWERS COMPARABLE TO THE ISOLATED SBO EXPERIMENTS THAT OPERATED PRIMARILY IN THE $5\pi/6$ MODE

Q	Isolated-SBO Dominant Mode	Isolated-SBO Power (MW)	HRPM Dominant Mode	HRPM Power (MW)
440	$5\pi/6$	9.8 ± 1.7	π	9.5 ± 1.4
240	$5\pi/6$	18 ± 5	π	19 ± 6
140	$5\pi/6$	37 ± 12	π	28 ± 9

most strongly. More often, the $5\pi/6$ mode was dominant, and thus, its data are presented in ellipses, where the height and width indicate the spread from several shots. On the other hand, the $4\pi/6$ mode appeared seldom enough that it suffices to present the composite frequency of each shot individually, as Xs.

For each shot, a single composite frequency is determined as the arithmetic mean of the three waveguide outputs, in the same process that was implemented for the HRPM. The center of each ellipse is located at the arithmetic mean of all composite frequencies from a cluster of shots operating in the $5\pi/6$ mode at a given magnetic field. The width and height of each ellipse represent one standard deviation in the magnetic field and composite frequency measurements, respectively. Therefore, smaller ellipses represent data with little spread. A total of 50, 77, and 64 shots were taken with the aperture length set to 28 mm (h_1), 32 mm (h_2), and 36 mm (h_3), respectively. In each set of experiments, the total number of shots was distributed evenly among the magnetic fields tested.

The experiments demonstrated that the SBO $5\pi/6$ mode was consistently the dominant operating state. For each aperture length, the composite output frequency on most shots agreed best with the $5\pi/6$ mode cold test frequency. At h_1, the $5\pi/6$ mode was dominant on every shot, whereas at h_2 and h_3, it was dominant on 74% and 75% of the shots, respectively. At h_2 and h_3, the $4\pi/6$ mode located at 1.98 and 1.95 GHz was observed on 20% and 15% of shots, respectively. The remainder of the shots (6% at h_2 and 10% at h_3) demonstrated a large degree of mode competition such that one frequency would be dominant in one output waveguide, while another would be dominant in the other two. Thus, on these shots, the composite frequency was bounded between the two modes previously discussed. These data points are excluded from Fig. 7(a) because it is not obvious that they agree with any of the cold test mode frequencies, but this is only because there is strong mode competition between the $4\pi/6$ and $5\pi/6$ modes. Again, the π-mode was not observed as a dominant mode in the isolated SBO configuration.

Fig. 7(b) presents the isolated SBO output power parameterized as a function of magnetic field and h. Each data point represents a set of shots tested at one magnetic field, although there was a small amount of spread in the magnetic field measurements. Therefore, these data points are centered at the arithmetic mean of the sets of peak output power and magnetic field. For each set clustered at one mean magnetic field, the standard deviation was calculated for the output power and magnetic field measurements. The vertical and horizontal error bars, thus, extend one standard deviation from the arithmetic mean for these clusters. The greater values

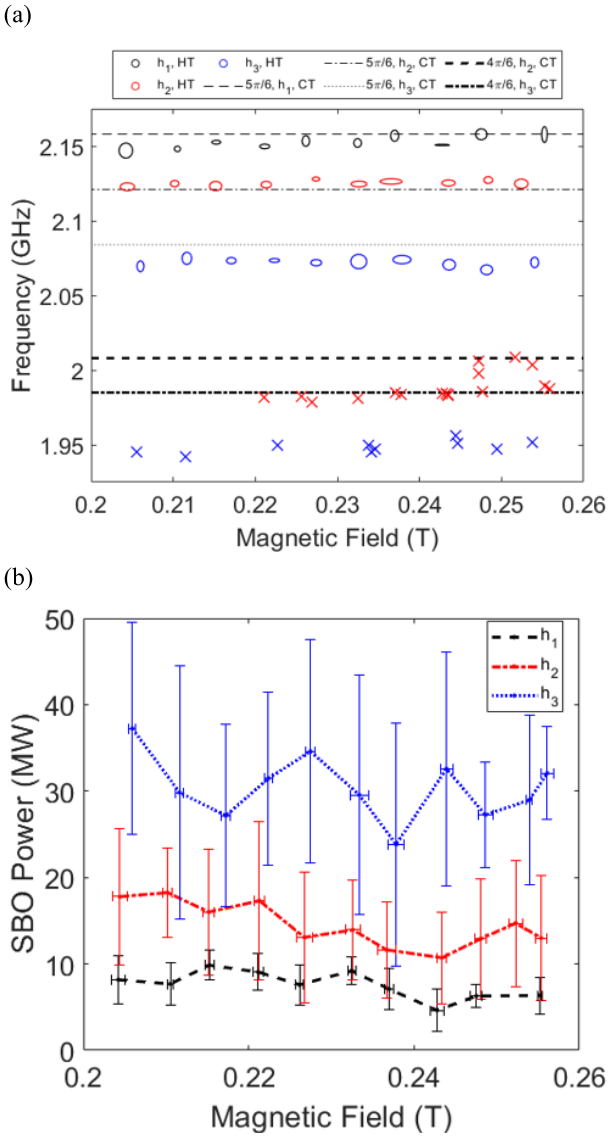

Fig. 7. (a) Composite output frequency information for the isolated SBO configuration is displayed in the form of ellipses and crosses as a function of the magnetic field and aperture length h. Each ellipse is centered at the arithmetic mean of the magnetic field and power measurements for a set of shots demonstrating $5\pi/6$ mode operation, while each X represents the composite frequency and magnetic field measurements for individual shots operating in the $4\pi/6$ mode. The height and width of each ellipse represent one standard deviation of the composite frequency and magnetic field measurements for the sets of shots operating in the $5\pi/6$ mode, respectively. Significantly, the π-mode was not observed. The $5\pi/6$ mode was dominant in the majority of shots for each value of h. (b) Output power is given as a function of magnetic field and h. The data points are located along the ordinate at the arithmetic mean of the output power for all shots at a given magnetic field. Vertical and horizontal error bars extend one standard deviation in either direction. The output power was observed to increase as h was increased.

of h yielded increased output powers. At h_1, h_2, and h_3, the highest output powers are 9.9 $\pm$ 1.7 MW, 18 $\pm$ 5.2 MW, and 37 $\pm$ 12 MW, at magnetic fields of 0.215, 0.210, and 0.206 T, respectively. These are compared to HRPM operation in Table II, which is given Section III.

In the low Q_t experiments, the isolated SBO operated at an instantaneous peak efficiency of 18% $\pm$ 8% at the optimal magnetic field for power generation, while the HRPM had an efficiency of 9% $\pm$ 2% at the optimal tuner position. This is defined as the ratio of the SBO power to the cathode power, each measured at the time of peak microwave power generation. The cathode power is defined as the product of current entering the magnetron and the applied voltage. It is suspected that a large amount of current becomes endloss, emitted from the tops of the planar cathode, so the electronic efficiency may be higher. The amount of endloss has not been experimentally measured, but physical hardware such as cables have been damaged and destroyed due to the presence of axial currents in the chamber. Cathode endloss could be improved by using materials better suited to insulate emission. The efficiency could also be improved by further decreasing the quality factor. In the HRPM, it is speculated that the SBO could operate at a Q_t even lower than possible in the isolated SBO. Here, the LBO would act as a driving oscillator that, with its harmonic content, promotes the SBO to start when it otherwise could not oscillate in isolation [27].

The efficiency could also be improved by extracting from the LBO. The isolated SBO demonstrates a greater efficiency than the HRPM likely in part because the LBO is not present. In the HRPM, the LBO draws current, but none of its power is extracted. Thus, efficiency could be improved with the implementation of extraction on the LBO. However, this could perhaps be detrimental to the device. It is possible that the highly repeatable output frequencies observed in Fig. 5(c) are enabled because the LBO is itself a comparatively high Q oscillator. As a high Q oscillator, its frequency does not drift, but if its quality factor was decreased then the LBO would likely impart a greater range of harmonic frequencies upon the SBO, resulting in output frequencies with greater variance. Additionally, it is unclear how extraction would affect harmonic content in the hub and consequently the kinetic interaction between the oscillators. Implementation of extraction on the LBO would be of significant importance in a subsequent prototype.

Despite the fact that the application of (3) appeared to be appropriate for the π-mode, this does not appear to be the case for the $5\pi/6$ mode. As shown in Table I, the $5\pi/6$ Q_t remains relatively constant as a function of h, which suggests the output power in this mode should not increase as h is increased but rather remain the same. Although this is not understood, the fact that the $5\pi/6$-mode output power increases as h increases suggests that Q_{ext} is indeed inversely proportional to h. This is only possible if, according to (3), Q_u is proportional to h for the $5\pi/6$ mode, but it is unclear why that would be. Because operation of the HRPM experiments primarily concerns the π-mode, this result was not pursued further.

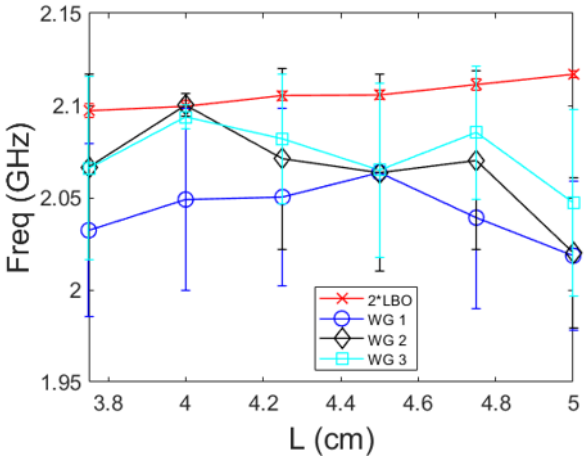

Fig. 8. Average LBO harmonic frequency and individual waveguide frequencies over L for the low Q_t reverse magnetic field experiment. By reversing the magnetic field, harmonic frequency locking is significantly reduced. This is the expected result, because the harmonic content in the LBO-modulated electron hub would diminish as it travels a much larger distance to reach the SBO.

V. HRPM Experiments With Reversed Magnetic Field

To further examine the nature of the locking mechanism between the two oscillators, an experiment was performed with the magnetic field oriented in the reverse direction. By reversing the magnetic field, the electron hub flows from the SBO to LBO. If the locking mechanism was indeed the beam, the oscillators would be less likely to lock with the reverse beam because PIC simulations show that harmonic content dissipates as the space charge spoke travels around both recirculating bends and the opposing planar drift region. As an example, this is demonstrated in Fig. 1, where the spokes from the SBO are almost nonexistent after traveling around the first recirculating bend. If the behavior shown in Fig. 5(c) is still observed with the reverse beam, then perhaps the two structures are locking due to coupled electromagnetic fields or some global mode between them, instead of the beam.

This experiment was performed with aperture length set to h_3, or low Q_t, and the results are shown in Fig. 8. The legend adopts the terminology "WG N," where N represents the waveguide physically closest to the LBO. For example, WG 1 is the nearest to the LBO, while WG3 is the farthest away. A total of 35 shots were taken to complete this experiment, distributed evenly among six different tuner positions.

In this experiment, the waveguide outputs' demonstrated behavior so varied that each was separated in the analysis. While the LBO was unaffected by the change in magnetic field direction, the SBO frequency significantly varied on a shot-to-shot basis.

Furthermore, there is no longer a clear trend between the LBO harmonic frequency and SBO waveguide frequencies. The output from WG 1 significantly disagrees with the LBO harmonic frequency across the entire range of L. WG 2 and 3 are in significant disagreement with the LBO harmonic frequency as well, except for when L is set to 4 cm. Interestingly, at this point, the output frequencies from WG 2 and 3 appear to

lock to the LBO harmonic, but this interaction ceases in WG 1. This point aside, the strong interaction between oscillators observed in Fig. 5(c) was not observed, and it is concluded that harmonic frequency locking is not demonstrated with a reversed magnetic field.

VI. Conclusion

The HRPM is a multifrequency oscillator designed to advance the state of the art in high-power multifrequency sources. The HRPM demonstrated oscillation at L-band and S-band simultaneously by implementing two planar oscillators adjacent to each other in the RPM geometry, leaving a smooth-bore drift region on the opposite side of the cathode. This smooth-bore drift region could feasibly be replaced with a pair of oscillators scaled to two other frequencies, enabling greater multispectral capabilities in a subsequent prototype. Additionally, each oscillator is frequency agile due to the leveraging of harmonic frequency locking. Multiple SBO quality factors and LBO excitation frequencies were examined to determine their effects on output power and the nature of the harmonic frequency-locked state. When tested in isolation, the SBO was observed to operate primarily in the $5\pi/6$ mode, whereas the HRPM demonstrated π-mode operation. This shows that the introduction of the LBO can be used as a method of mode control when tuned properly. Furthermore, the SBO output power did not significantly change between the isolated SBO and HRPM experiments. Finally, the SBO demonstrated operation consistent with the driven oscillator hypothesis implemented in the design of the HRPM. Reversing the magnetic field eliminated harmonic frequency locking, which further validates the coupling mechanism for harmonic frequency locking in magnetrons is indeed harmonic content in the beam spokes.

References

[1] G. B. Collins, *Microwave Magnetrons*. New York, NY, USA: McGraw-Hill, 1948.

[2] R. J. Barker, J. H. Booske, N. C. Luhmann Jr., and G. S. Nusinovich, *Modern Microwave and Millimeter-Wave Power Electronics*. Piscataway, NJ, USA: Wiley, 2005.

[3] R. J. Barker and E. Schamiloglu, *High-Power Microwave Sources and Technologies*. New York, NY, USA: IEEE Press, 2001.

[4] D. Andreev, A. Kuskov, and E. Schamiloglu, "Review of the relativistic magnetron," *Matter Radiat. at Extremes*, vol. 4, no. 6, Nov. 2019, Art. no. 067201, doi: 10.1063/1.5100028.

[5] E. C. Okress, *Crossed-Field Microwave Devices*. New York, NY, USA: Academic Press, 1961.

[6] G. Bekefi and T. J. Orzechowski, "Giant microwave bursts emitted from a field-emission, Relativistic-Electron-Beam magnetron," *Phys. Rev. Lett.*, vol. 37, no. 6, pp. 379–382, Aug. 1976, doi: 10.1103/PhysRevLett.37.379.

[7] A. Palevsky and G. Bekefi, "Microwave emission from pulsed, relativistic e-beam diodes. II. the multiresonator magnetron," *Phys. Fluids*, vol. 22, no. 5, p. 986, 1979, doi: 10.1063/1.862663.

[8] T. A. Treado, W. O. Doggett, G. E. Thomas, R. S. Smith, J. Jackson-Ford, and D. J. Jenkins, "Operating modes of relativistic rising-sun and a6 magnetrons," *IEEE Trans. Plasma Sci.*, vol. 16, no. 2, pp. 237–248, Apr. 1988, doi: 10.1109/27.3820.

[9] J. S. Levine, B. D. Harteneck, and H. D. Price, "Frequency-agile relativistic magnetrons," *Proc. SPIE*, vol. 2557, pp. 74–79, Sep. 1995, doi: 10.1117/12.218536.

[10] J.-C. Ju, Y.-W. Fan, H.-H. Zhong, and T. Shu, "A novel dual-frequency magnetically insulated transmission line oscillator," *IEEE Trans. Plasma Sci.*, vol. 37, no. 10, pp. 2041–2047, Oct. 2009, doi: 10.1109/TPS.2009.2027603.

[11] J. Cai, X. Wu, and J. Feng, "Traveling-wave tube harmonic amplifier in terahertz and experimental demonstration," *IEEE Trans. Electron Devices*, vol. 62, no. 2, pp. 648–651, Feb. 2015, doi: 10.1109/TED.2014.2377914.

[12] A. M. Elfrgani, S. Prasad, M. I. Fuks, and E. Schamiloglu, "Dual-band operation of relativistic BWO with linearly polarized Gaussian output," *IEEE Trans. Plasma Sci.*, vol. 42, no. 8, pp. 2141–2145, Aug. 2014, doi: 10.1109/TPS.2014.2331334.

[13] R. M. Gilgenbach, Y.-Y. Lau, D. M. French, B. W. Hoff, J. Luginsland, and M. Franzi, "Crossed field device," U.S. Patent 8 841 867 B2, Sep. 23, 2014.

[14] R. M. Gilgenbach, Y.-Y. Lau, D. M. French, B. W. Hoff, M. Franzi, and J. Luginsland, "Recirculating planar magnetrons for high-power high-frequency radiation generation," *IEEE Trans. Plasma Sci.*, vol. 39, no. 4, pp. 980–987, Apr. 2011, doi: 10.1109/TPS.2010.2099670.

[15] M. A. Franzi *et al.*, "Recirculating-Planar-Magnetron simulations and experiment," *IEEE Trans. Plasma Sci.*, vol. 41, no. 4, pp. 639–645, Apr. 2013, doi: 10.1109/TPS.2013.2242493.

[16] G. B. Greening, N. M. Jordan, S. C. Exelby, D. H. Simon, Y. Y. Lau, and R. M. Gilgenbach, "Multi-frequency recirculating planar magnetrons," *Appl. Phys. Lett.*, vol. 109, no. 7, Aug. 2016, Art. no. 074101.

[17] G. B. Greening, *Multi-Frequency Recirculating Planar Magnetrons*. Ann Arbor, MI, USA: Univ. Michigan, 2017.

[18] G. B. Greening, S. C. Exelby, D. A. Packard, N. M. Jordan, Y. Y. Lau, and R. M. Gilgenbach, "Harmonic frequency locking in the multifrequency recirculating planar magnetron," *IEEE Trans. Electron Devices*, vol. 65, no. 6, pp. 2347–2353, Jun. 2018, doi: 10.1109/TED.2018.2810240.

[19] D. A. D. Greenwood, "An ICEPIC convergence study using a relativistic magnetron," AFRL, Albuquerque, NM, USA, Tech. Memorandum TM-2005-1005, May 2005.

[20] R. E. Peterkin and J. W. Luginsland, "A virtual prototyping environment for directed-energy concepts," *Comput. Sci. Eng.*, vol. 4, no. 2, pp. 42–49, 2002, doi: 10.1109/5992.988646.

[21] M. Franzi *et al.*, "Coaxial all cavity extraction in the recirculating planar magnetron," in *Proc. IEEE Int. Vac. Electron. Conf.*, Apr. 2014, pp. 89–90, doi: 10.1109/IVEC.2014.6857504.

[22] W. D. Kilpatrick, "Criterion for vacuum sparking designed to include both rf and DC," *Rev. Sci. Instrum.*, vol. 28, no. 10, pp. 824–826, Oct. 1957, doi: 10.1063/1.1715731.

[23] Y. Y. Lau *et al.*, "A re-examination of the Buneman–Hartree condition in a cylindrical smooth-bore relativistic magnetron," *Phys. Plasmas*, vol. 17, no. 3, Mar. 2010, Art. no. 033102, doi: 10.1063/1.3328804.

[24] T. Isenlik and K. Yegin, "Tutorial on the design of Hole-Slot-Type cavity magnetron using CST particle studio," *IEEE Trans. Plasma Sci.*, vol. 41, no. 2, pp. 296–304, Feb. 2013, doi: 10.1109/TPS.2012.2235466.

[25] E. L. Ginzton, *Microwave Measurements*. New York, NY, USA: McGraw-Hill, 1957.

[26] P. J. Petersan and S. M. Anlage, "Measurement of resonant frequency and quality factor of microwave resonators: Comparison of methods," *J. Appl. Phys.*, vol. 84, no. 6, pp. 3392–3402, Sep. 1998, doi: 10.1063/1.368498.

[27] T. A. Treado, P. D. Brown, and D. Aiguier, "New experimental results at long pulse and high repetition rate, from Varian's phase-locked magnetron array program," in *Proc. Intense Microw. Pulses*, Los Angeles, CA, USA, Jul. 1993, pp. 241–251, doi: 10.1117/12.147464.

Drew A. Packard (Student Member, IEEE) received the B.S.E and M.S.E degrees in nuclear engineering and radiological sciences from the University of Michigan, Ann Arbor, MI, USA, in 2016 and 2017, respectively, where he is currently pursuing the Ph.D. degree.

As a Graduate Student performing research on high-power microwave devices under the mentorship of Prof. Gilgenbach with the Plasma, Pulsed Power, and Microwave Laboratory (PPPML), he specializes in crossed field devices. During his time with the PPPML, he has simulated, designed, and tested magnetrons, crossed field amplifiers, and magnetically insulated line oscillators (MILOs). He has completed two internships with L-3 Communications, Electron Devices Division, San Carlos, USA. His general research interests include charged particle beams, accelerators, diode physics, beam–wave interaction, RF sources and engineering, antennas, high-power microwaves, pulsed power, simulation techniques, and general electromagnetic phenomena.

Steven C. Exelby (Student Member, IEEE), photograph and biography not available at the time of publication.

Nicholas M. Jordan (Senior Member, IEEE) received the B.S.E., M.S.E., and Ph.D. degrees in nuclear engineering and radiological science from the University of Michigan, Ann Arbor, MI, USA, in 2002, 2004, and 2008, respectively.

From 2008 to 2013, he was with Cybernet Systems, Ann Arbor, MI, USA, where he developed technology to disable uncooperative vehicles using microwave pulses. He is currently an Associate Research Scientist with the Plasma, Pulsed Power, and Microwave Laboratory, University of Michigan. His current research interests include high-power microwave devices, pulsed power, laser ablation, Z-pinch physics, and plasma discharges.

Christopher J. Swenson (Student Member, IEEE) received the B.S.E. and M.S.E. degrees in nuclear engineering and radiological sciences from the University of Michigan, Ann Arbor, MI, USA, in 2018 and 2019, respectively, where he is currently pursuing the Ph.D. degree under the supervision of Prof. R. Gilgenbach in the PPPML, with a focus on the testing of high-power magnetrons and the design of other cross field devices such as amplifiers and MILOs.

He has had internships at Knolls Atomic Power Laboratory, Niskayuna, NY, USA, in the Nuclear Analysis Group and at L3Harris Technologies in Menlo Park, CA, USA, with the Electron Devices Division.

Brad W. Hoff (Senior Member, IEEE) received the B.S. degree in physics from U.S. Naval Academy, Annapolis, MD, USA, in 1999 and the M.S.E. degree in nuclear engineering, the M.S.E. degree in electrical engineering, and the Ph.D. degree in nuclear engineering from the University of Michigan, Ann Arbor, MI, USA, in 2006, 2007, and 2009, respectively.

He is currently a Senior Research Physicist with the Directed Energy Directorate, Air Force Research Laboratory, Kirtland Air Force Base, Albuquerque, NM, USA.

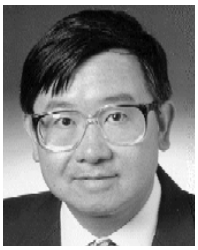

Y. Y. Lau (Fellow, IEEE) received the B.S., M.S., and Ph.D. degrees in electrical engineering from the Massachusetts Institute of Technology, Cambridge, MA, USA, in 1968, 1970, and 1973, respectively.

He is currently a Professor with the University of Michigan, Ann Arbor, MI, USA, where he specialized in RF sources, heating, and discharge.

Dr. Lau was an Elected Fellow of the American Physical Society in 1986. He received the 1999 IEEE Plasma Science and Applications Award and the 2017 IEEE John R. Pierce Award for Excellence in Vacuum Electronics. He served three terms as an Associate Editor for the *Physics of Plasmas* from 1994 to 2002.

Ronald M. Gilgenbach (Life Fellow, IEEE) received the B.S. and M.S. degrees from the University of Wisconsin—Madison, Madison, WI, USA, in 1972 and 1973, respectively, and the Ph.D. degree in electrical engineering from Columbia University, New York, NY, USA, in 1978.

He spent several years as a Member of the Technical Staff with Bell Telephone Labs, Holmdel, NJ, USA, in the mid-1970s. From 1978 to 1980, he performed gyrotron research with the Naval Research Laboratory, Washington, DC, USA, and also performed the first electron cyclotron heating experiments on tokamak plasma in the USA with the Oak Ridge National Laboratory, Oak Ridge, TN, USA. In 1980, he joined as a Faculty Member with the University of Michigan (UM), Ann Arbor, MI, USA, where he became the Director of the Plasma, Pulsed Power and Microwave Laboratory. He has supervised 51 graduated Ph.D. students with UM. He has collaborated in research with scientists at the Air Force Research Laboratory, Kirtland AFB, NM, USA, Sandia National Laboratories, Albuquerque, NM, USA, NASA Glenn, Cleveland, OH, USA, Northrop-Grumman, Rolling Meadows, IL, USA, L-3 Communications, Williamsport, PA, USA, General Motors Research Labs, Warren, MI, USA, the Los Alamos National Laboratory, Los Alamos, NM, USA, Fermilab, Batavia, IL, USA, the Naval Research Laboratory, and the Institute of High Current Electronics, Tomsk, Russia. He is currently the Chihiro Kikuchi Collegiate Professor with the Department of Nuclear Engineering and Radiological Sciences, UM. He has authored or coauthored some 200 articles in refereed journals and books. He holds five patents granted.

Dr. Gilgenbach is a fellow of the American Physical Society Division of Plasma Physics. He was a recipient of the NSF Presidential Young Investigator Award in 1984, the Plasma Sciences and Applications Committee (PSAC) Award from the IEEE in 1997, and the Peter Haas Pulsed Power Award from IEEE in 2017. He served as the IEEE PSAC Chair from 2007 to 2008. He was an Associate Editor of the *Physics of Plasmas* journal.